

High-spatial resolution long-mid-infrared observations of massive star-forming regions: Local star formation sequence

Mizuho UCHIYAMA ^{1,*} Takashi MIYATA,² Shigeyuki SAKO ²,
 Takafumi KAMIZUKA,² Kentaro ASANO,² Tomohiko NAKAMURA,^{2,3}
 Takuya YAMASHITA,⁴ Takuya FUJIYOSHI,⁵ Mizuki YONEDA,⁶ Masahiro KONISHI,²
 Shintaro KOSHIDA,⁵ Kentaro MOTOHARA ⁴, Toshihiko TANABÉ,²
 Yutaro KITAGAWA,² Ken TATEUCHI,² and Yuzuru YOSHII^{2,7}

¹Institute of Space and Astronautical Science, Japan Aerospace Exploration Agency, 3-1-1 Yoshinodai, Chuo-ku, Sagami-hara, Kanagawa 252-5210, Japan

²Institute of Astronomy, Graduate School of Science, The University of Tokyo, 2-21-1 Osawa, Mitaka, Tokyo 181-0015, Japan

³Department of Astronomy, Graduate School of Science, The University of Tokyo, 7-3-1 Hongo, Bunkyo-ku, Tokyo 113-0033, Japan

⁴National Astronomical Observatory, 2-21-1 Osawa, Mitaka, Tokyo 181-8588, Japan

⁵Subaru Telescope, National Astronomical Observatory of Japan, 650 North A'ohoku Place, Hilo, HI 96720, USA

⁶Tadano Ltd., Advanced Technology Research center, 2217-13 Hayashi-cho, Takamatsu, Kagawa 761-0301, Japan

⁷Steward Observatory, University of Arizona, 933 North Cherry Avenue, Rm. N204, Tucson, AZ 85721-0065, USA

*E-mail uchiyoama@ir.isas.jaxa.jp

Received 2021 June 22; Accepted 2021 October 2

Abstract

The formation of massive stars in dense and cold molecular clouds is a fundamental problem in star formation. In this work, we studied three compact massive star-forming regions, M8E, RAFGL 6366S, and IRAS 18317–0513, to investigate the environment of massive star formation, specifically the possibility of a local feedback process. Our new mid-infrared observations using miniTAO/MAX38 at 31 and 37 μm resolved individual objects in each region and allowed us to obtain their individual luminosities and masses. Together with existence/absence of ultra-compact H II regions, it is suggested that less-massive objects are more evolved than the more-massive objects in two out of the three regions. Because the objects that are more massive evolve faster, those that are less massive form earlier. This formation trend of local mass-sequential star was first suggested in 0.1 pc-scale massive star-forming regions. Therefore, feedback, such as outflows, jets, or radiative heating, from previously formed lower-mass young stellar objects might affect the environment of parental clouds and lead to next-generation massive young stellar objects.

Key words: stars: formation — stars: individual (M8E, RAFGL 6366S, IRAS 18317–0513) — stars: massive

1 Introduction

Massive stars with masses larger than $8 M_{\odot}$ are crucial sources for dynamic and chemical evolution of the universe. They provide a strong ultraviolet (UV) radiation field and supply significant mechanical energy through powerful outflows, jets, and supernova explosions (Zinnecker & Yorke 2007). Observational and theoretical studies have revealed that massive stars form in massive, dense, and cold molecular clouds (McKee & Tan 2002; Peretto & Fuller 2009; Tan et al. 2014). During the formation, massive stars remain embedded in the parental massive cores even when they reach the zero-age main sequence (ZAMS) stages. The formation process of massive young stellar objects (MYSOs), especially their mass growth process and surrounding environment, has not yet been fully elucidated, although observations using radio interferometers reveal the inner structures of some MYSOs (Tan et al. 2014, and references therein).

Studying the star-forming sequence is a unique method for understanding the process of massive star formation. To determine which object is formed first in massive star-forming regions and thus study star-forming sequences, the evolutionary stages and masses of individual objects are required. This is because a more massive young stellar object (YSO) forms and evolves faster regardless of mass accretion processes (McKee & Tan 2002; Bonnell & Bate 2006; Zinnecker & Yorke 2007). For instance, large pc-scale (about 5 pc or larger) star-forming sequences between massive YSOs and low-mass YSOs, which start from outer regions containing lower-mass YSOs to inner regions containing higher-mass YSOs, have been reported in some star-forming clusters such as S255 and G34.43+00.24 (Wang et al. 2011; Foster et al. 2014; Peretto et al. 2020). This sequence requires mechanisms that affect the environment of star-forming clouds, and some previous studies have suggested the effect of competitive accretion on massive cluster-forming clouds (Wang et al. 2011; Peretto et al. 2020).

However, star-forming sequences in massive star-forming regions that are more compact, approximately 0.1 pc scale or less, which include several YSOs and would be affected more directly and strongly by the feedback from the neighbors, were not investigated. Although the distribution of the evolutionary stage and possible changes from the initial environment were indicated in some early-stage massive star-forming regions using dust and molecular tracer observations at millimeter wavelengths (e.g., Qiu et al. 2011; Wang et al. 2012; Stephens et al. 2015; Liu et al. 2020), the trend of the star-forming sequence has not been well studied until now; hence, the possible local effects and feedback have not been studied either. In addition, observations at millimeter wavelengths exhibit dust continuum

emission from massive cores, not from massive YSOs inside the cores. Because the mass of the entire core does not fall on to the YSO, the star-forming sequences between YSOs cannot be derived from radio observations of massive cores directly.

For MYSOs, their evolutionary stages, pre-hydrogen burning or main sequence stages, can be roughly distinguished by the absence or presence of hyper-compact (HC) H II or ultra-compact (UC) H II regions via radio free-free emissions. The masses of YSOs, including MYSOs, inside the cores could be derived from their bolometric luminosities using stellar models (Thompson 1984; Cox 2000). However, it is difficult to estimate their individual bolometric luminosities accurately because generally MYSOs are deeply embedded in their surrounding envelopes, and their apparent temperatures are approximately as low as 100 K (Churchwell 2002; Sridharan et al. 2002; Grave & Kumar 2009; Issac et al. 2020). This corresponds to the mid-infrared (MIR) and far-infrared (FIR), and the spatial resolution of observations at these wavelengths is limited, especially at longer wavelengths. Therefore, observations in the long-MIR, which ranges from 25 to $40 \mu\text{m}$ in this study, or longer wavelengths with high spatial resolution (less than $10''$) that is sufficient to resolve individual objects, are essential for deriving bolometric luminosities and thus star-forming sequences in small regions.

In this study, we carried out observations using a ground-based MIR instrument to achieve sufficient spatial resolution in the long-MIR, which allowed us to first derive luminosities and masses of individual YSOs in three compact massive star-forming regions with a few $\times 0.1$ pc size. We have investigated star-forming sequences in the observed regions and discussed possible origins of the obtained sequences and feedback processes in the small massive star-forming regions.

Details of the target selection, observational status, and data reduction are presented in section 2. The results of the photometry and estimation of individual luminosities and masses are described in section 3. Possible explanations for the observed differences in evolutionary stages, including mass-sequential star formation, are discussed in section 4. Additionally, we discuss possible mechanisms that indicate mass-sequential star formation. Finally, the conclusions are presented in section 5.

2 Observations

2.1 miniTAO/MAX38

All measurements were made using the Mid-infrared Astronomical eXplorer 38 (MAX38; Nakamura et al. 2010; Asano et al. 2012) mounted on the now hibernated 1.0 m

Table 1. Filter properties of MAX38.

Filter	λ [μm]	$\Delta\lambda$ [μm]	Measured FWHM of PSF
8.9 μm	8.9	0.8	2".4
12 μm	12.2	0.5	3".2
18 μm	18.7	0.9	4".9
25 μm	24.5	1.9	6".3
31 μm	31.7	2.2	7".6
37 μm	37.3	2.4	8".5

miniTAO telescope (Minezaki et al. 2010). The miniTAO telescope is located at the summit of Mt. Chajnantor in Chile at an altitude of 5640 m, which provides (perhaps apart only from Antarctica) the best conditions for ground-based astronomical observations in the long-MIR. MAX38 employs a 128×128 Si:Sb blocked impurity band (BIB) array detector with a pixel scale of $1''.26$, offering a field of view of $2.0 \times 2.5 \text{ arcmin}^2$ (the remaining $0.5 \times 2.5 \text{ arcmin}^2$ is reserved for spectroscopy). The properties of the filters used in this study and spatial resolution of each band are listed in table 1. In longer-MIR, the spatial resolution in our observations was $7''.6$ at $31 \mu\text{m}$ and $8''.5$ at $37 \mu\text{m}$. The $31 \mu\text{m}$ and $37 \mu\text{m}$ filters are metal mesh filters developed for the miniTAO/MAX38 (Sako et al. 2012), and our observations using the miniTAO/MAX38 achieved the highest spatial resolutions for all the observed regions in the long-MIR. Detailed descriptions of the telescope and instrument can be found in the references cited above.

2.2 Target selection

In this study, we observed three massive star-forming regions, namely M8E, RAFGL 6366S, and IRAS 18317–0513, from an initial list of candidates fulfilling the following criteria:

- To study the local star-forming sequence and the local feedback, the regions must contain at least two objects (MYSOs and/or sources associated with H II regions) within a few $\times 0.1 \text{ pc}$ region studied in the Red MSX Source (RMS) survey (Lumsden et al. 2013) or in de Wit et al. (2009).
- Sufficient archival data must exist for the construction of spectral energy distributions (SEDs), and radio (preferably high spatial resolution interferometric) observations at centimeter wavelengths must have been made for all of them to establish whether they have reached the main sequence or not.
- To search the possible local (about 0.1 pc) feedback in detail, the regions do not indicate large-scale (about 5 pc or larger) cloud–cloud collision; the velocity profile of the molecular cloud does not show multiple components.

2.3 Observations

Table 2 summarizes our observations. The weather conditions were reasonable with the precipitable water vapor (PWV) measured using the nearby Atacama Pathfinder Experiment (APEX; Güsten et al. 2006) having a range of 0.35 to 1.05 mm (see tables 2 and 3). This resulted in a transmittance in the long-MIR of 30% or more considering each band profile of the observing filter. A standard chop–nod technique (e.g., Papoular 1983; Kaeufl et al. 1991) was used. The chopping/nodding frequency was adjusted according to the night conditions. Corresponding throws (distances) were employed so that the chopped/nodded beams would not overlap as we employed on-chip chop–and–nod (i.e., all four chopped/nodded beams are on the detector). The chopping/nodding parameters are summarized in tables 2 and 3.

Point spread functions (PSFs) are crucial for separating multiple sources in crowded regions or revealing extended structures. Therefore, we also observed bright infrared stars selected from the IRAS Point Source Catalogue. They are listed in table 3 and are hereinafter referred to as “PSF standards.” The target objects and PSF standards were observed at the same wavelengths on the same night. Most PSF standards are well-known evolved stars that exhibit extended structures at shorter wavelengths. We confirmed that all, except one, were point sources at the spatial resolution of miniTAO/MAX38. We could not find any information regarding the spatial extent of V1185 Sco in the literature. However, as it is located much further away ($d = 1.2 \text{ kpc}$; Yuasa et al. 1999) than the star of a similar (Mira) type in our sample, WX Psc ($d \gtrsim 190 \text{ pc}$), which is unresolved at $\sim 13 \mu\text{m}$ (Lagadec et al. 2011), we treat it as a point source in this study.

2.4 Data reduction

2.4.1 Co-adding chopping and nodding beams using weighted average method

While making MIR observations using ground telescopes, a standard on-chip chop–and–nod subtraction method is generally used to eliminate large sky emissions and detect fluxes of the target objects. In this study, we obtained the standard on-chip chop–and–nod data, and the above method was used for sky background subtraction at as long as $25 \mu\text{m}$. However, at 31 and $37 \mu\text{m}$, the sky emission immediately varies, and this frequently results in a residual sky pattern in simply chop–and–nod subtracted images. Therefore, the “weighted average method” (Nakamura 2011; Nakamura et al. 2016) is used to eliminate this residual sky pattern. This method creates a good sky frame for every object frame among the chop–and–nod beam frames, which minimizes the residual sky pattern by weighted

Table 2. Observing conditions of the targets.

Region	Date in UT [yyyy/mm/dd]	Filter	PSF Standards	Int. time [s]	PWV* [mm]	Airmass	Chopping throw
M8E	2010/09/20	31 μm	IRC +10420	1100	0.60	1.08	32''
		18 μm	IRC +10420	100	0.60	1.18	
	2011/05/27	37 μm	V1185 Sco	4000	0.45	1.03	38''
		25 μm	IRC +10420	1000	0.50	1.27	
RAFG 63665	2011/10/31	31 μm	VY CMa	1000	0.85	1.41	20''
		18 μm	VY CMa	500	0.85	1.40	
		12 μm	VY CMa	500	0.85	1.48	
	2011/11/01	8.9 μm	WX Psc	200	0.85	1.50	20''
	2012/10/24	25 μm	α Ori	1600	0.40	1.52	38''
		37 μm	α Ori	1600	0.45	1.41	
IRAS 18317–0513	2011/11/04	31 μm	IRC +10420	1500	0.35	1.06	20''
		18 μm	IRC +10420	600	0.35	1.07	
		12 μm	IRC +10420	1000	0.35	1.05	

*The PWV values were obtained from APEX weather data archive (<http://www.apex-telescope.org/weather/>) and modified to the values of the observing site using the method shown in Miyata et al. (2012) and Konishi et al. (2015).

Table 3. Observing conditions of the PSF standards.

Object	Date in UT [yyyy/mm/dd]	Filter	Int. time [s]	PWV* [mm]	Airmass	Chopping throw
IRC+10420 [†]	2010/09/19	31 μm	500	0.60	1.23	32''
		18 μm	100	0.60	1.23	
	2011/05/27	25 μm	100	0.50	1.43	38''
	2011/11/04	31 μm	200	0.35	1.21	20''
		18 μm	50	0.35	1.22	
		12 μm	50	0.35	1.22	
V1185 Sco [‡]	2011/5/27	37 μm	1000	0.45	1.03	38''
VY CMa [§]	2011/10/31	31 μm	100	0.85	1.00	20''
		18 μm	100	0.85	1.00	
		12 μm	10	0.85	1.00	
WX Psc	2011/11/01	8.9 μm	10	1.05	1.50	20''
α Ori [#]	2012/10/24	25 μm	100	0.50	1.22	38''
		37 μm	600	0.50	1.19	

*PWV values were obtained from APEX weather data archive (<http://www.apex-telescope.org/weather/>) and modified to the values of observing site using the method shown in Miyata et al. (2012) and Konishi et al. (2015).

[†]Mid-A type massive red supergiant.

[‡]Mira (O-rich).

[§]Massive red supergiant.

^{||}Late-M type AGB star (O-rich).

[#]M2 type O-rich supergiant.

superposition of the other frames. The weight coefficients of the individual frames were determined to minimize the residual sky pattern of the object frame after subtraction. The detailed method and algorithms are described in Nakamura (2011) and Nakamura et al. (2016). After the subtraction, all four images of the objects in the chop-and-nod subtracted images were added to create a single object image.

2.4.2 Flux calibration

Flux calibration against non-variable standard stars was obtained from Cohen et al. (1999); however, they were

simply too faint for miniTAO/MAX38 at wavelengths longer than 18 μm . At longer wavelengths, we extrapolated the calibration of PSF standards in the *N*-band derived from the Cohen standard stars using the MIR colors derived from the Infrared Space Observatory/Short Wavelength Spectrometer (ISO/SWS) data. Although the PSF standards are well-known variables, their MIR colors are stable and change by only up to 5% over a three-year period (Monnier et al. 1998). V1185 Sco was not observed by Monnier, Geballe, and Danchi (1998), but the typical MIR color variation of Mira-type stars could be less than 10% (Smith et al. 2002). Therefore, it is considered a non-variable in the MIR.

Table 4. Calibrated flux densities of the PSF standards.

PSF standard	Observing band	Flux density [Jy]	Calibrator	Calibrated band
WX Psc	8.9 μm	850	π^2 Aqr	8.9 μm
VY CMa	12 μm	9600	β Col	12 μm
	18 μm	12000		
	31 μm	5100		
α Ori	25 μm	790	Jupiter	31 μm
	31 μm	550		
	37 μm	370		
IRC+10420	12 μm	1100	α Boo	18 μm
	18 μm	2300		
	25 μm	2400		
	31 μm	1900		
V1185 Sco	18 μm	630	α Boo	18 μm
	37 μm	1100		

Because α Ori was only observed at 25, 31, and 37 μm , the extrapolation method could not be applied. Therefore, we adopted the flux density of Jupiter at 31 μm observed on the same night. Cosmic Background Explorer/Diffuse Infrared Background Experiment (COBE/DIRBE) measurements of the planet at 25 and 60 μm were interpolated and scaled using an apparent diameter, assuming that the brightness temperature of Jupiter is constant. The overall uncertainty in flux calibration is estimated to be $\lesssim 10\%$. The flux densities of the PSF standards are listed in table 4.

The transmission/emission of MIR sky varies rapidly and significantly. We used the ATRAN model (S. D. Lord 1992)¹ to examine the fluctuations in atmospheric transmittance. Although the PWV value doubled from 0.5 to 1.0 mm, the transmittance decreased by less than 10% and 30% at 18 and 25 μm , respectively. However, the situation at longer wavelengths (i.e., at 31 and 37 μm) is quite different and changes more significantly. Asano et al. (2012) established that there is a strong correlation between the apparent brightness of a star and that of the sky background. When the sky becomes more opaque, the sky background increases while transmitted stellar light gets reduced. The ATRAN model was also used to estimate the fluctuation in the sky background. We assumed that 30% of the total background radiation comes from the telescope and the rest comes from the sky (see Asano et al. 2012 for details). Generally, the uncertainty from the fluctuation in the sky transmittance is $\lesssim 30\%$. The only exceptions are the 31 and 37 μm images of RAFGL 6366S, which suffer from an uncertainty of approximately 80%. In addition, the 25 μm flux calibration of RAFGL 6366S suffers from a large uncertainty because its PSF standard star (α Ori, also used for flux calibration) was observed under poor weather conditions.

3 Results

3.1 Mid-infrared morphology

3.1.1 M8E

M8E is a massive star-forming region located at the south-eastern edge of M8. Figure 1 shows images of M8E at 18, 25, 31, and 37 μm with PSF reference stars, which show beam patterns for point sources at individual bands. A bright object is detected and clearly resolved into two sources at 25 μm , and the extended structure around them is detected at 31 and 37 μm . The separation of the two peaks is $7''.7$, and the position angle is 45° . At 18 μm , the extended structure is marginal, much fainter than that at 25 μm , but not like a point source. The characteristics of the morphology and the source subtraction process are described in detail in the next subsection.

Previous high-spatial-resolution (less than $1''$) MIR images obtained at 24.5 μm using the Subaru/Cooled Mid Infrared Camera and Spectrometer (COMICS) (de Wit et al. 2009; Linz et al. 2009) have shown that this region has three sources: a compact and bright MYSO, M8E-IR; a cometary-shaped object with a UCH II region, M8E-radio (Simon et al. 1984); and a much fainter previously undetected source. The positions of the three objects are shown in figure 1b. This comparison indicates that the two peaks resolved in the 25 μm image correspond to M8E-IR and M8E-radio. Note that slight differences in positions (less than $1''$) are indicated by comparison, although they are significantly smaller than the spatial resolution of miniTAO/MAX38 ($6''.3$ at 25 μm). No sources corresponding to the third object (shown as a triangle mark) were found in our images. This is because of the insufficient sensitivity of miniTAO/MAX38. Although details of the third object are unclear, its non-detection at 31 and 37 μm suggests that it is a much less massive object rather than a less-evolved MYSO or an edge-on MYSO. This is because such objects usually have a red color and could be detected in the long-MIR (Grave & Kumar 2009). Therefore, this third object will not be discussed in detail due to it being out of the mass range that is focused on here.

3.1.2 RAFGL 6366S

RAFGL 6366S is a massive star-forming region and is considered a part of the Gemini OB1 molecular complex (Carpenter et al. 1995). Figure 2 shows images of RAFGL 6366S at 8.9, 12, 18, 25, 31, and 37 μm , together with images of the PSF reference stars including WX Psc, VY CMa, and α Ori. Two sources are clearly observed at 25 μm , while only a single extended object is detected at 31 and 37 μm . The images of the PSF references at 31 and 37 μm were slightly elongated; this could be because of the imperfect focusing of the telescope. However, the target images were more elongated compared to the PSF images,

¹ S. D. Lord 1992, NASA Technical Memorandum 103957 (<https://ntrs.nasa.gov/api/citations/19930010877/downloads/19930010877.pdf>).

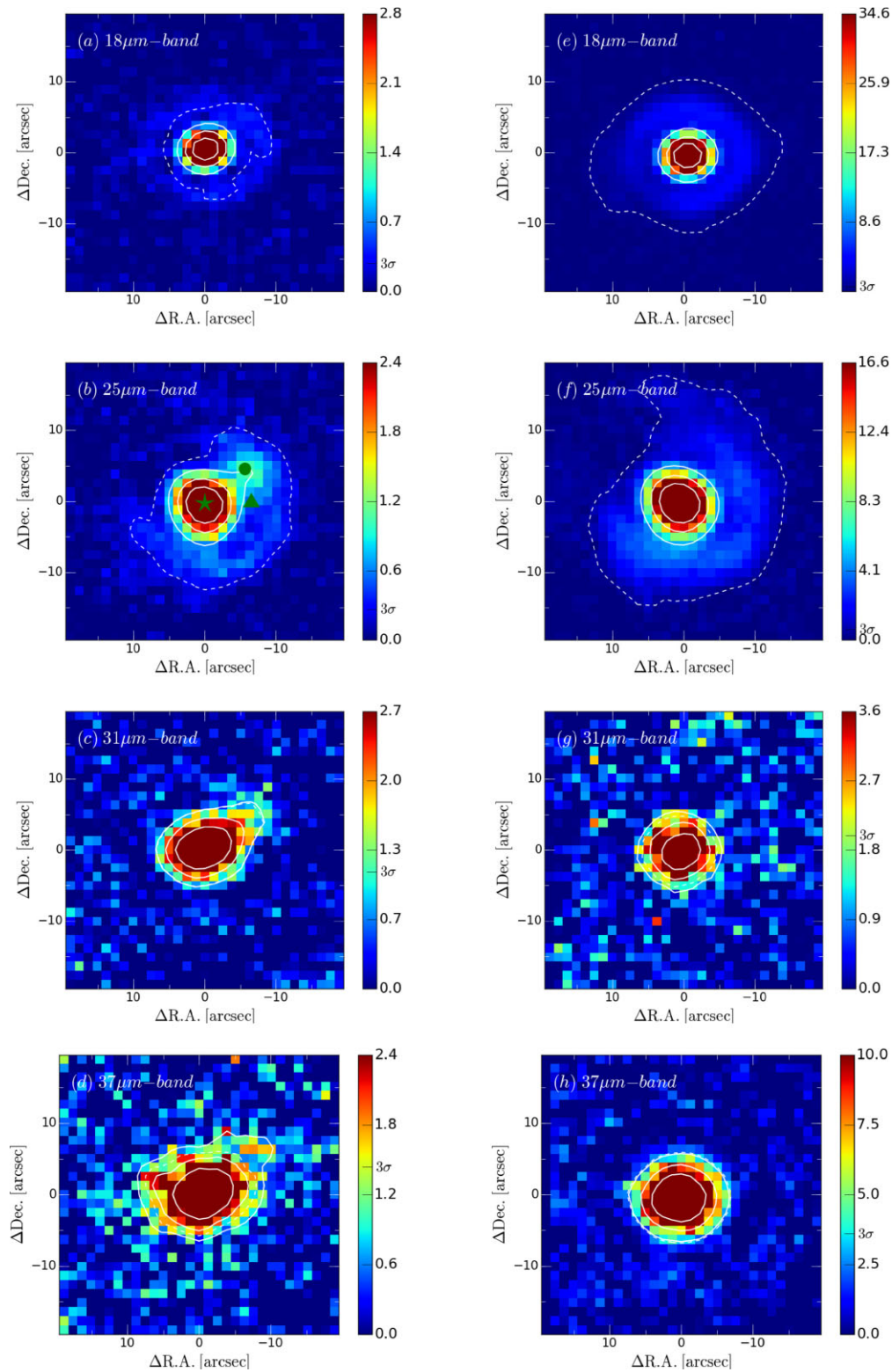


Fig. 1. MIR images of M8E (left) and PSF standard (right) observed using the MAX38. The field of view is $40'' \times 40''$ in all images, and north is up. The center position of each image corresponds with its peak. The unit represented in color-scale is $[\text{Jy arcsec}^{-2}]$. The images of M8E in panels (a), (b), (c), and (d) correspond to images of 18, 25, 31, and $37 \mu\text{m}$, respectively. The images of PSF standards in panels (e), (f), (g), and (h) correspond to images of 18, 25, 31, and $37 \mu\text{m}$, respectively. The PSF standards are IRC +10420 in panels (e), (f), and (g) and V1185 Sco in panel (h). Dashed lines represent the 3σ contours of background noise. Solid lines represent the 20%, 40%, and 60% contours of the peak counts. At all wavelengths, a structure extending to the north-west can be observed in M8E compared with the PSF standards. In panel (b), the filled star, circle, and triangle marks indicate the positions of M8E-IR, M8E-radio, and the third brightest source of M8E at $24.5 \mu\text{m}$ as described in de Wit et al. (2009), assuming that the peak at $25 \mu\text{m}$ corresponds to the position of the brightest object, M8E-IR. (Color online)

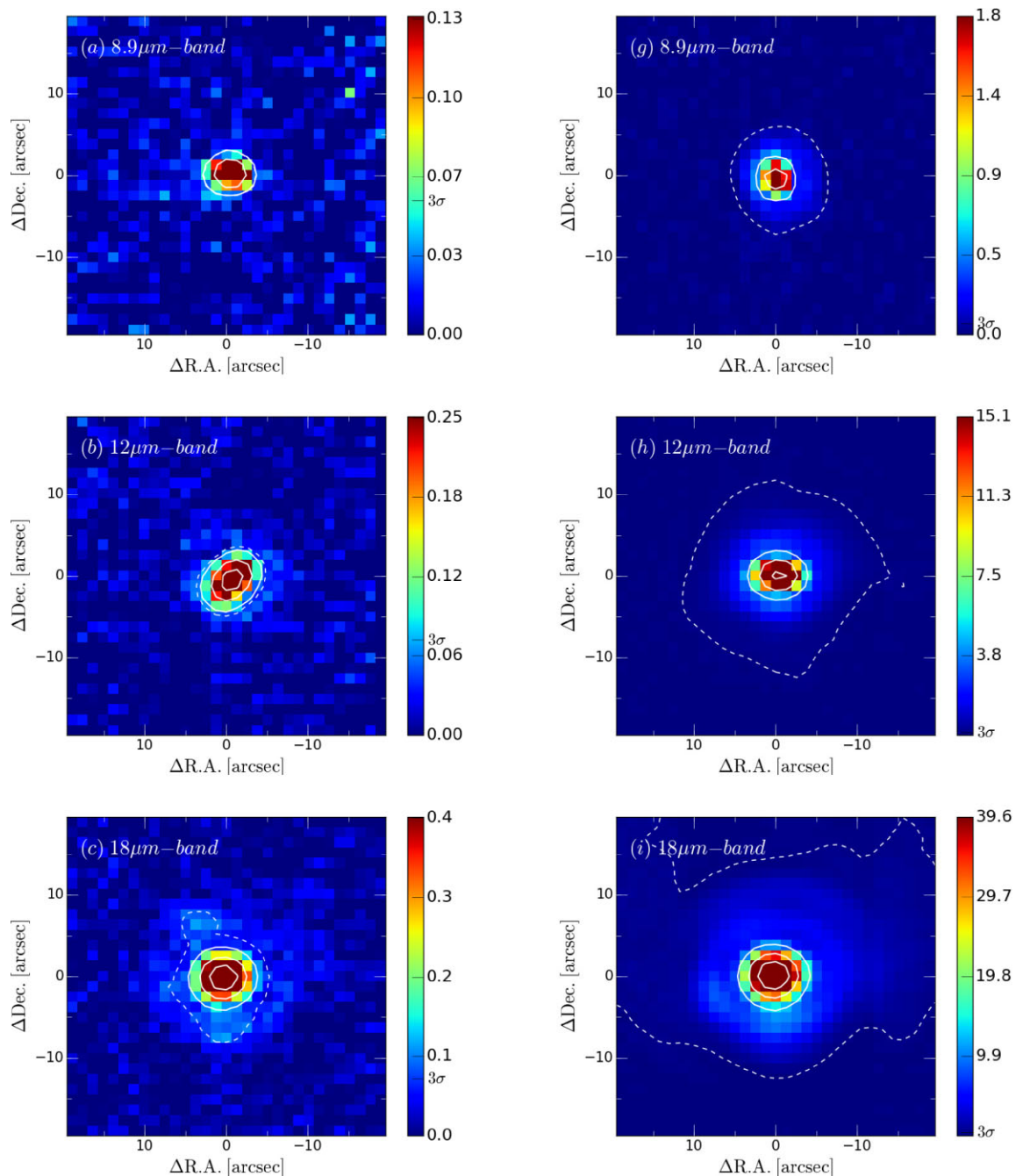


Fig. 2. MIR images of RAFGL 6366S (left) and PSF standard (right) observed with the MAX38. The field of view is $40'' \times 40''$ in all images, and north is up. The center position of each image corresponds with its peak. The unit represented in color-scale is Jy arcsec^{-2} . The images of RAFGL 6366S in panels (a), (b), (c), (d), (e), and (f) correspond to images of 8.9, 12, 18, 25, 31, and $37 \mu\text{m}$, respectively. The images of PSF standards in panels (g), (h), (i), (j), (k), and (l) correspond to images of 8.9, 12, 18, 25, 31, and $37 \mu\text{m}$, respectively. Because neither RAFGL 6366S nor the PSF standard have a high signal-to-noise ratio in the $37 \mu\text{m}$ images, 2 pixel \times 2 pixel binning was performed on both images. PSF standards are WX Psc in panel (g); VY CMa in panels (h), (i), and (k); and α Ori in panels (j) and (l). Dashed lines represent the 3σ contours of background noise. Solid lines represent the 20%, 40%, and 60% contours of the peak counts. In panels (c), (d), (e), and (f), a structure extending to the north-east can be observed in RAFGL 6366S. In panel (d), the filled star, circle, triangle, and square marks indicate the positions of a MYSO (RAFGL 6366S-IR1), a UCH II (RAFGL 6366S-IR2), a NIR object, and an IR-dark core detected in Rodon (2009), respectively, assuming that the peak at $25 \mu\text{m}$ corresponds to the position of the brightest object at millimeter wavelengths, MYSO. (Color online)

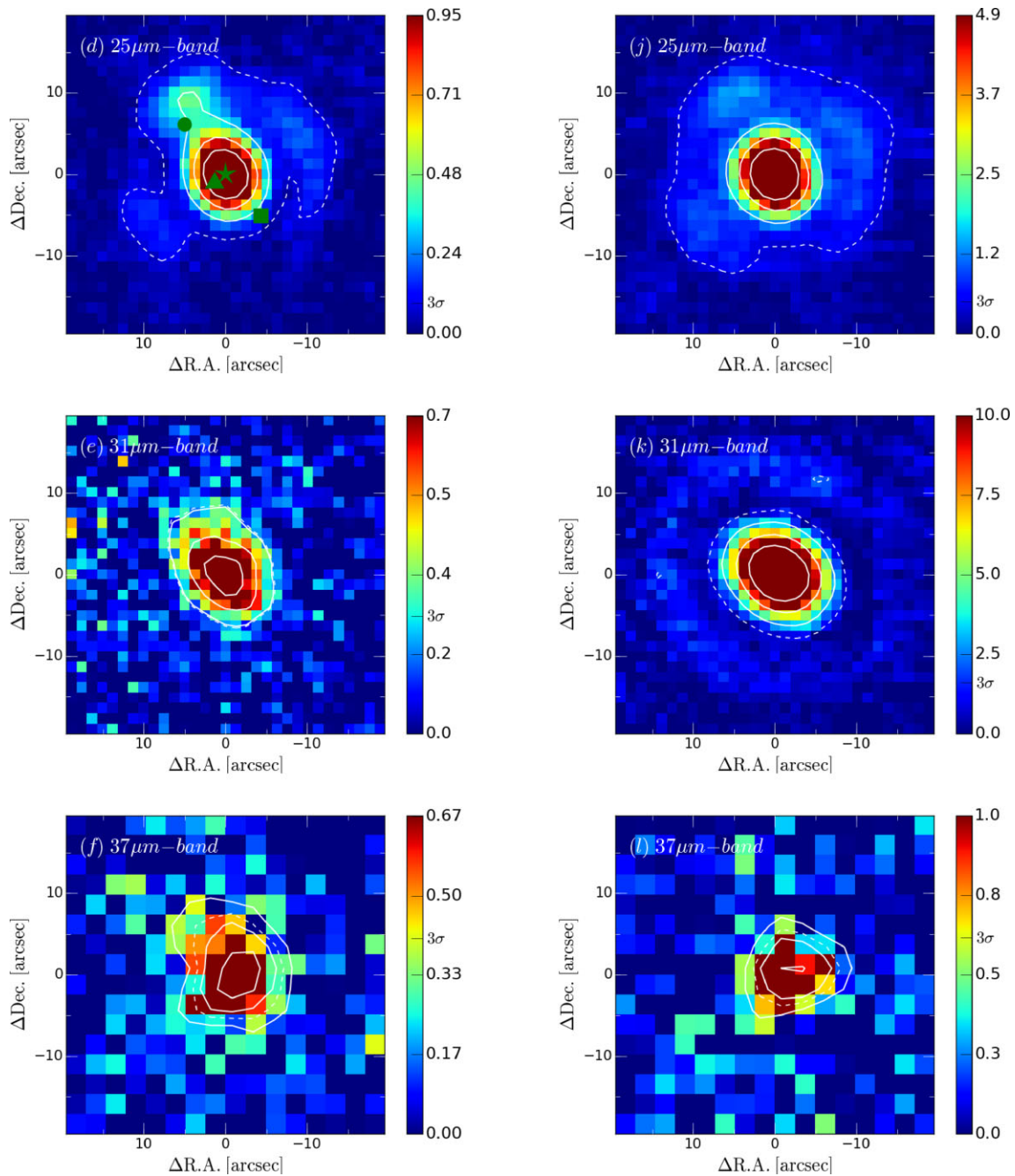


Fig. 2. (Continued)

and they would not be artificial but real (the sources' splitting process will be discussed in detail in the next subsection). The separation of the two peaks is $8''$ at $25\ \mu\text{m}$. In the $18\ \mu\text{m}$ image, the source has an extended structure in almost the same direction as that in the $25\ \mu\text{m}$ image. In the $12\ \mu\text{m}$ image, the source is clearly elongated; however, its direction differs from that in the $25\ \mu\text{m}$ images. It might be caused by non-detection of the fainter object to the north-north-east due to sensitivity and higher spatial resolution than longer wavelengths, which possibly resolve the

central brighter object. At $8.9\ \mu\text{m}$, the detected source was a single point-like source. Hereinafter, the central brighter source and the fainter source to the north-north-east are referred to as RAFGL 6366S-IR1 and RAFGL 6366S-IR2, respectively.

Previous observations in the millimeter, MIR, and near-infrared (NIR) ranges with higher spatial resolution (less than $5''$) have revealed that this region consists of four sources: an object with a UCH II region, an MYSO, an NIR object, and an IR-dark core (Motttram et al. 2007;

Rodon 2009; Lumsden et al. 2013). Rodon (2009) reported that the MYSO is associated with molecular SiO outflow, indicating massive accretion, whereas the NIR object is not; it is considered a low-mass YSO. Their positions are marked in figure 2d. The previous MIR image of the region at $11.2\ \mu\text{m}$ obtained with Gemini North/Michelle in the RMS project shows two sources: a fainter point-like source and a brighter source with an extended structure (Mottram et al. 2007; Lumsden et al. 2013). Their positions correspond well with those of the object with the UCH II region and the MYSO in Rodon (2009), although the image cannot resolve the MYSO or the NIR object. This could be because of insufficient spatial resolution, and their flux ratio is not determined either. Compared with the $25\ \mu\text{m}$ image, the positions of the object with the UCH II region and the MYSO correspond to those of IR2 and IR1. However, our observations cannot distinguish the NIR object from the MYSO in IR1 at $18\ \mu\text{m}$ and longer wavelengths owing to insufficient spatial resolution and/or sensitivity. Note that the slight difference in positions compared with the previous works may be attributed to the position of the diffraction ring of the instrument. We could not find an MIR object corresponding to the IR-dark core, which was not detected in the previous MIR image at $11.2\ \mu\text{m}$ either.

IR1 is partly spatially resolved into two sources of the MYSO and the NIR object at $12\ \mu\text{m}$, and its shape resembles that of the previous MIR image at $11.2\ \mu\text{m}$ (Lumsden et al. 2013). However, it is not detected at $8.9\ \mu\text{m}$, possibly because of the strong extinction of silicate towards the MYSO. Because of the insufficient sensitivity of MAX38, IR2 cannot be observed at 8.9 and $12\ \mu\text{m}$.

3.1.3 IRAS 18317–0513

IRAS 18317–0513 is an infrared-bright massive star-forming region (Bronfman et al. 1996; Faúndez et al. 2004). Figure 3 shows images of IRAS 18317–0513 and the PSF reference star, IRC +10420, at 12 , 18 , and $31\ \mu\text{m}$. The target shows extended structure at 12 , 18 , and $31\ \mu\text{m}$. Two NIR objects have been detected in observations with a higher spatial resolution of less than $2''$ (Urquhart et al. 2009). One is brighter in the NIR and N -band and the other is located southeast of the brighter one (Lumsden et al. 2013). Free-free emission at the centimeter wavelengths has not been reported in this region, and both objects seem to be MYSOs (Urquhart et al. 2009). Their positions are marked in figure 3b. The two marked positions are consistent with the elongated structure seen in the $18\ \mu\text{m}$ image. Hereinafter, the objects on the northwestern and southeastern sides are referred to as IRAS 18317–0513-IR1 and IRAS 18317–0513-IR2, respectively.

3.2 PSF photometry and flux measurements

Two MIR sources were detected in each observed region. To obtain the flux densities of the individual sources accurately, PSF photometry was performed (Nakamura 2012). First, we obtained the flux density ratios of the two detected sources through PSF fitting. The relative position measured in other bands was used when the fainter source was not clearly resolved and its position was difficult to determine. The measured flux-density ratios of the two detected sources are listed in table 5. The flux densities of the two sources were calibrated from those of the PSF standards. To evaluate the validity of the PSF fitting, best-fitting model images were obtained from the superposition of the two best-fitted PSFs. They were subtracted from the observed images, and the residual images were checked. For instance, the resultant images of IRAS 18317–0513 at $12\ \mu\text{m}$ are shown in figure 4. No artificial sources above 3σ of background noise were observed in the source-located area of the subtracted image. In addition, the standard deviation of the subtracted residual images in the object-subtracted area (σ_{resid}) is approximately equal to that in the background sky area (σ_{bg}), as summarized in table 5. These results indicate that the fitting was conducted properly. However, the RAFGL 6366S image at $12\ \mu\text{m}$ shows a significantly large standard deviation. This could be because RAFGL 6366S-IR1 shows an elongated structure in the opposite direction when compared to the other wavelengths at $12\ \mu\text{m}$, as shown in figure 2b. The obtained flux densities are listed in table 6. When the second source is not detected, the upper limit of the flux is obtained from a flux density of $3\sigma_{\text{resid}}$. The flux density errors in table 6 include photometric errors from statistical origins, but not systematic errors from the instability of atmospheric transmittance. For M8E, spectral data obtained by the ISO/SWS is available. The beam size of ISO/SWS is $14'' \times 27''$ and M8E-IR and M8E-radio have not been spatially resolved. In comparison with those obtained from the sum of the M8E-IR and M8E-radio data, the difference is 1.2%, 4.4%, 20%, and 25% at 18 , 15 , 31 , and $37\ \mu\text{m}$, respectively. These differences could be explained by the expected instability of the atmospheric transmittance, as discussed in section 2. We considered that the derived flux densities do not suffer from unexpected additional systematic errors because of the consistency between ISO/SWS and our data. The flux densities of M8E-IR and M8E-radio derived from ISO/SWS data and our flux ratios are listed in table 6. In M8E, the ISO/SWS flux densities were used for the following analysis to eliminate systematic errors caused by the variation of the atmospheric transmittance, which is not large but also not negligible.

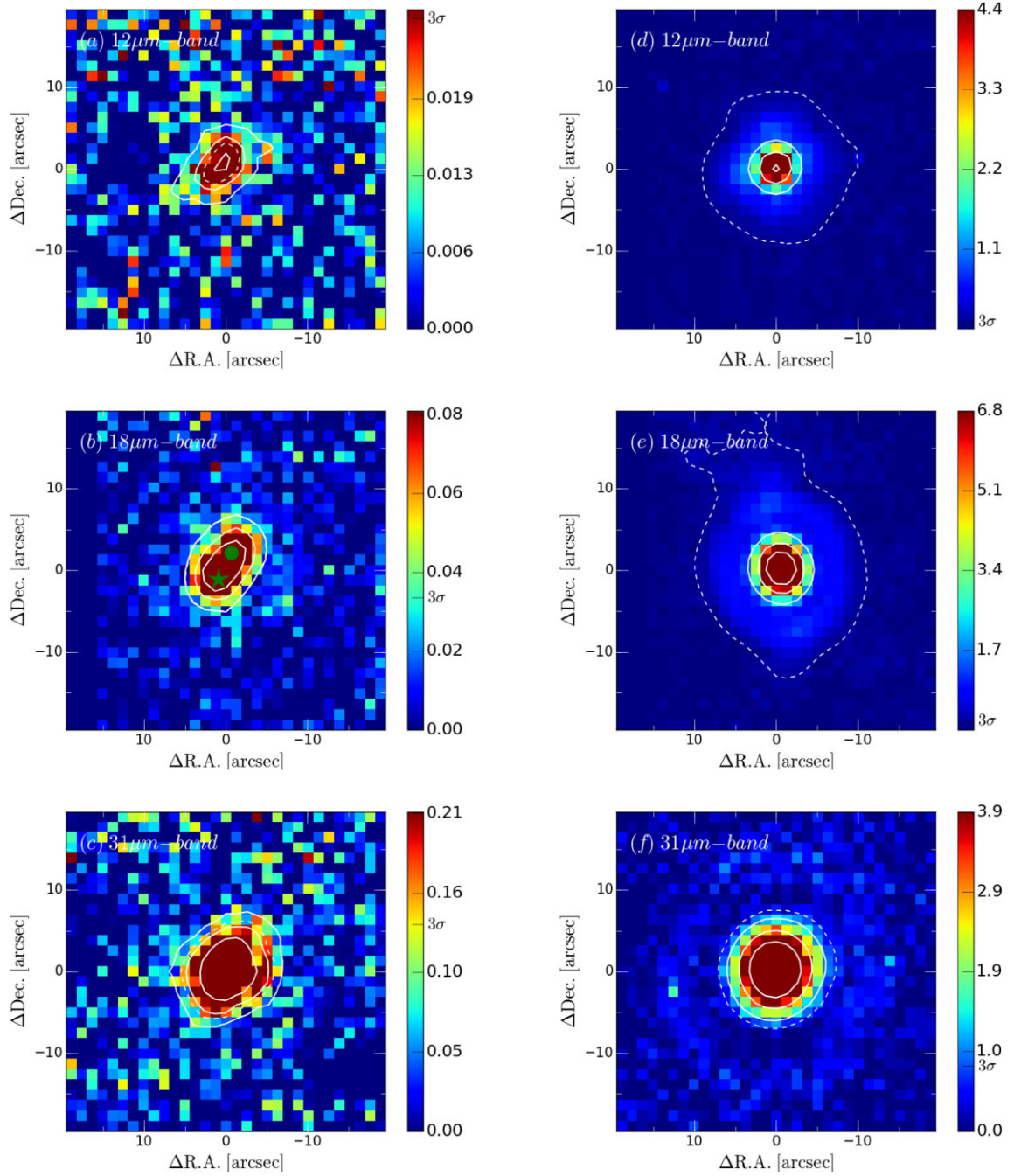


Fig. 3. MIR images of IRAS 18317–0513 (left) and PSF standard (right) observed using the MAX38. The field of view is $40'' \times 40''$ in all images, and north is up. The center position of each image corresponds with its peak. The unit represented in color-scale is Jy arcsec^{-2} . The images of IRAS 18317–0513 in panels (a), (b), and (c) correspond to images of 12, 18, and $31 \mu\text{m}$, respectively. The images of PSF standards panels (d), (e), and (f) correspond to images of 12, 18, and $31 \mu\text{m}$, respectively. The PSF standards are IRC +10420 at all wavelengths. Dashed lines represent the 3σ contours of background noise. Solid lines represent the 20%, 40%, and 60% contours of the peak counts. At all wavelengths, a structure extending to the north-west can be clearly observed in IRAS 18317–0513 as compared with the PSF standards. In panel (b), the filled star mark represents the brightest NIR object (IRAS 18317–0513-IR1) from a previous work Urquhart et al. (2009) and the filled circle mark represents the second-brightest one (IRAS 18317–0513-IR2), assuming that the peak at $18 \mu\text{m}$ corresponds to the position of the brighter NIR object. (Color online)

3.3 Estimation of luminosities and masses

To obtain star-forming sequences in the observed regions, the masses and evolutionary stages of the individual objects are required. For an object with a UCH II region, we assume

that its current luminosity is equal to its ZAMS bolometric luminosity, and its corresponding spectral type and mass are obtained from the stellar parameters in Thompson (1984) and Cox (2000). Note that the observed luminosity of

Table 5. Result of the PSF photometry.

Object	Filter	Flux ratio*	$\sigma_{\text{resid}}^{\dagger}$ [mJy arcsec ⁻²]	$\sigma_{\text{bg}}^{\ddagger}$ [mJy arcsec ⁻²]
M8E	18 μm	0.028 ± 0.006	63	60
	25 μm	0.14 ± 0.01	94	57
	31 μm	0.24 ± 0.03	320	330
	37 μm	0.23 ± 0.02	310	360
RAFGL 6366S	8.9 μm	0.03 ± 0.03	40	37
	12 μm	0.03 ± 0.08	76	49
	18 μm	0.07 ± 0.03	69	60
	25 μm	0.1 ± 0.1	40	34
	31 μm	0.21 ± 0.03	330	330
	37 μm	0.31 ± 0.06	690	690
IRAS 18317–0513	12 μm	0.36 ± 0.02	19	18
	18 μm	1.2 ± 0.1	35	33
	31 μm	1.3 ± 0.1	140	140

*The flux ratios of M8E-radio to M8E-IR, RAFGL 6366S-IR2 to RAFGL 6366S-IR1, and IRAS 18317–0513-IR2 to IRAS 18317–0513-IR1 are listed.

$\dagger\sigma_{\text{resid}}$ represents “Standard deviation of object-subtracted residual area”.

$\ddagger\sigma_{\text{bg}}$ represents “Background sky standard deviation”.

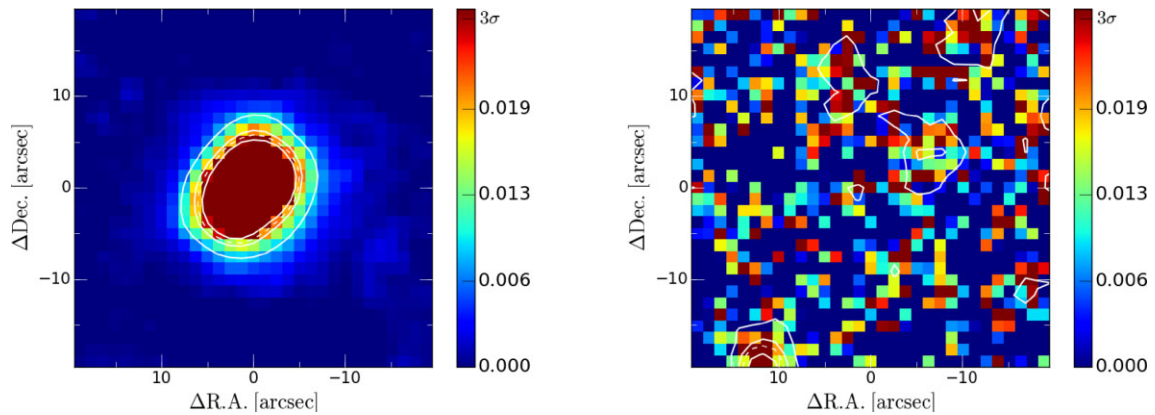


Fig. 4. Images of two-component best-fitting model of IRAS 18317–0513 at 12 μm . The derived best-fitting model image (left) and subtracted image from the observed image (right) are shown. The field of view is $40'' \times 40''$ in all images, and north is up. The center positions of the images correspond to the peaks of the original observed image. The unit represented in color-scale is [Jy arcsec⁻²]. Dashed lines represent the 3σ contours of the background noise in the original observed image (shown in figure 3a). Solid lines represent the 20%, 40%, and 60% contours of the peak counts of the individual images. No artificial sources above 3σ are seen in the source-located area of the subtracted image, which suggests that the fitting is conducted properly. (Color online)

an object with a UCH_{II} region, which is the object after the contraction phase, may contain accretion luminosity. However, its fraction is approximately a tenth of the bolometric one, and this additional component is almost negligible for deriving stellar spectral type and mass (Hosokawa & Omukai 2009). For MYSO, a pre-H burning object, mass accretion is ongoing, and when the accretion rate is roughly constant, its luminosity including both bolometric and accretion luminosities, monotonously increases with time until the object reaches the ZAMS (Hosokawa & Omukai 2009). This indicates that its current luminosity corresponds to the lower limit at ZAMS. Therefore, the estimated mass derived from the current luminosity gives

a lower limit of the final mass of the MYSO under this assumption.

3.3.1 M8E

The spectral energy distributions of M8E-IR and M8E-radio are plotted in figure 5. The observed flux densities of M8E-IR and M8E-radio are almost consistent with those previously reported at 24.5 μm (de Wit et al. 2009). The SED of M8E-radio was fitted using single-temperature blackbody radiation. Most of the flux densities were well reproduced by the blackbody radiation at a temperature of 92 K (the solid line in figure 5) except for the flux density at 18 μm . The uncertainty of the temperature estimation

Table 6. Flux densities of the objects from photometry result given in Jy.

Filter	8.9 μm	12 μm	18 μm	25 μm	31 μm	37 μm
M8E-IR	—	—	183 ± 2	306 ± 3	436 ± 10	341 ± 6
	—	—	$185 \pm 2^*$	$293 \pm 3^*$	$364 \pm 8^*$	$455 \pm 8^*$
M8E-radio	—	—	5 ± 2	43 ± 3	107 ± 10	79 ± 6
	—	—	$5 \pm 2^*$	$41 \pm 3^*$	$89 \pm 8^*$	$105 \pm 8^*$
RAFGL 6366S-IR1	19.1 ± 0.6	52 ± 4	112 ± 4	164 ± 17	274 ± 7	260 ± 16
RAFGL 6366S-IR2	< 0.4	< 1.7	8 ± 4	22 ± 17	57 ± 7	81 ± 16
IRAS 18317–0513-IR1	—	6.4 ± 0.4	15.9 ± 0.7	—	53 ± 3	—
IRAS 18317–0513-IR2	—	2.3 ± 0.4	18.6 ± 0.7	—	69 ± 3	—

*Flux densities obtained from ISO/SWS spectral data of M8E. The flux density errors only include statistical origins and not systematic ones.

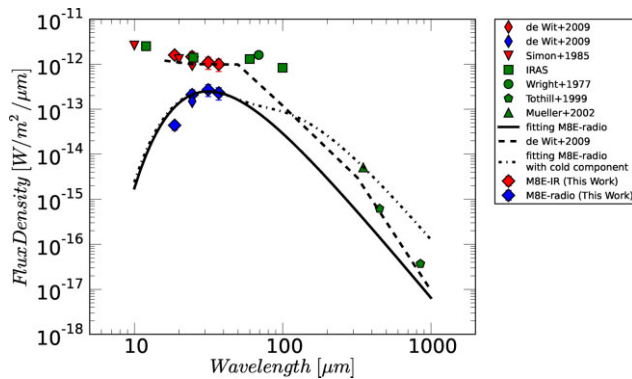


Fig. 5. SED of M8E. Red, blue, and green marks represent M8E-IR, M8E-radio, and unresolved flux densities, respectively. The data from this work is plotted using large diamond marks. The solid line represents the blackbody SED fitting of M8E-radio. The dashed line represents the SED fitting of M8E-IR by de Wit et al. (2009). The dash-dotted line represents the upper limit of the total luminosity of M8E-radio, together with the flux from the cold component in the sub-mm range. This flux from the cold component was fitted by 30 K blackbody radiation. (Color online)

is 4 K. The modeled flux density at 18 μm was approximately twice as high as the observed density. This could be attributed to the foreground extinction; however, the fitting cannot be improved when both the temperature and extinction are modified. Additionally, this could be due to a radial variation in density and temperature. However, a detailed model of the density and temperature radial structure cannot be created because of the insufficient number of separate observed flux densities of M8E-radio.

The distance of M8E from the Sun was measured using various methods (Tothill et al. 2008; Damiani et al. 2019). Tothill et al. (2008); Damiani et al. (2019) reported that the typical distance of M8E ranges from 1.3 to 1.8 kpc. In this study, 1.35 kpc, which was measured by Gaia, was adopted because it is the most reliable distance (Damiani et al. 2019). The luminosity of M8E-radio is $6.3 \times 10^2 L_{\odot}$, with an error of 15%. At wavelengths longer than 25 μm , the luminosity is estimated by integrating the blackbody at 92 K, whereas it is calculated by numerical integration of the

observed flux densities from 18 to 25 μm . The contribution at wavelengths shorter than 18 μm is negligible.

The flux from the FIR to the sub-millimeter (sub-mm) exhibit a significant contribution to the total flux. Cold components are generally associated with MYSOs and UCH II regions. They are extended diffuse clumps (Churchwell 2002). The temperature of the cold component is typically approximately 30 K, which is higher than that of the massive and dense starless molecular clouds (10–15 K) (Hofner et al. 2000; Kim & Koo 2001; Churchwell 2002). Therefore, the clumps were heated by the surrounding forming YSOs, including M8E-IR and M8E-radio, and the luminosity of the cold component should be considered in the possible total luminosity of the YSOs. However, it is unclear which of the YSOs—M8E-IR, M8E-radio, or the other non-detected lower-mass YSOs—makes a major contribution to heating. Therefore, the maximum and minimum (all and none) contribution of the cold component were calculated, and the upper and lower limits of the individual luminosities were obtained. Adopting a temperature of 30 K, the total luminosity of the cold component was estimated to be $7.3 \times 10^2 L_{\odot}$ (see the dash-dotted line in figure 5 for one of the possible cases of all the cold components associated with M8E-radio). The maximum flux density in the sub-mm and mm ranges obtained by Mueller et al. (2002) was used for the estimation because a possible maximum contribution is needed. The uncertainty of the luminosity is unclear; therefore, we adopted a relatively large error of 50%. This error corresponds to the temperature error of +3 K or –5 K. The total luminosity of the M8E-radio was derived to be $1.2 \pm 0.7 \times 10^3 L_{\odot}$.

Previously, de Wit et al. (2009) estimated the total luminosity of the same M8E region as $8 \times 10^3 L_{\odot}$ (derived from the dashed line in figure 5) using a distance of 1.8 kpc. This luminosity corresponds to $4 \times 10^3 L_{\odot}$ with a distance of 1.35 kpc. However, this has been based on unresolved photometric data at wavelengths longer than 25 μm , and it includes the luminosities of both M8E-IR and M8E-radio. Therefore, the luminosity of M8E-IR was estimated to be

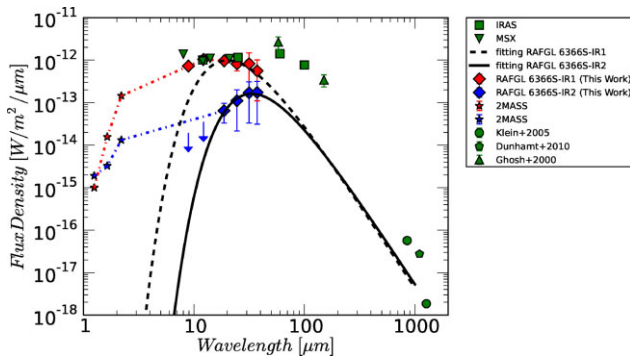


Fig. 6. Result of SED fitting to RAFGL 6366S IR1 and IR2. Red, blue, and green marks represent the flux densities of RAFGL 6366S-IR1, RAFGL 6366S-IR2, and the unresolved total RAFGL 6366S, respectively. The flux densities obtained are plotted using diamond marks. The solid line represents the blackbody radiation fitting of IR2 and the dotted line represents that of IR1. The blue dash-dotted line represents the linear fitting of IR2 flux densities at shorter wavelengths and the red one represents that of IR1. (Color online)

$2.8 \pm 0.7 \times 10^3 L_{\odot}$ by subtracting the estimated luminosity of M8E-radio.

M8E-radio is considered to be at near the ZAMS stage because M8E-radio has the UCH II region (Simon et al. 1984). Its spectral type is derived as B2.5-4 by the stellar model of Thompson (1984) using the derived luminosity ($1.2 \pm 0.7 \times 10^3 L_{\odot}$). This is slightly consistent with the estimation of the spectral type of B2 based on the measurement of the free-free emission reported by Simon et al. (1984). The mass is estimated as $6.0 \pm 1.0 M_{\odot}$ using the table of stellar parameters in Cox (2000). In contrast, M8E-IR does not reach the ZAMS stage because of the absence of a UCH II region (Walsh et al. 1998). The lower limit of the spectral type and mass of M8E-IR was estimated to be B1.5-2.5 and $8.0 \pm 0.5 M_{\odot}$ using the derived luminosity of $2.8 \pm 0.7 \times 10^3 L_{\odot}$ (Thompson 1984; Cox 2000). The above estimation shows that the less-massive object, M8E-radio, is located at a more evolved stage than the more-massive object, M8E-IR.

3.3.2 RAFGL 6366S

The SEDs of RAFGL 6366S-IR1 and RAFGL 6366S-IR2 are shown in figure 6. Considering that IR1 accounts for most of the flux densities, our flux densities are consistent with the flux densities previously unresolved by IRAS (12 and $25 \mu\text{m}$) and MSX (8, 12, 14, and $21 \mu\text{m}$). For IR1, the SED was well reproduced by a single-temperature blackbody radiation with a temperature of $145 \pm 9 \text{ K}$ (the dashed line in figure 6) at wavelengths longer than $25 \mu\text{m}$. In this study, $2.10 \pm 0.027 \text{ kpc}$ was adopted as the distance of RAFGL 6366S. This is the distance of S252, located in the same Gemini OB1 association (Carpenter et al. 1995), and it was obtained through parallax measurements using

VLBA (Reid et al. 2009). The derived luminosity of IR1 is $5.1 \times 10^3 L_{\odot}$ with an error of 24%. At wavelengths longer than $18 \mu\text{m}$, the SED of IR2 was well reproduced by a single-temperature blackbody radiation with a temperature of $87 \pm 3 \text{ K}$ (the solid line in figure 6). The derived luminosity of IR2 is $1.2 \times 10^3 L_{\odot}$, with an error of 17%. During the calculation, we ignored the upper limits of the flux density at 8.9 and $12 \mu\text{m}$ and used the linear interpolation between the flux densities in the K band and at $18 \mu\text{m}$ because the flux densities at 8.9 and $12 \mu\text{m}$ may suffer from severe silicate extinction.

The flux densities at FIR wavelengths ranging from 58 to $150 \mu\text{m}$ exhibit a significant excess over the fitted blackbody radiation. Because these were measured with large beam sizes of $>1'$, they may suffer from the contamination of the diffuse emission around the RAFGL 6366S core. Conversely, the sub-mm and mm flux densities at $750 \mu\text{m}$, 1.1 mm, and 1.3 mm were measured using smaller apertures of $31''$ and $15''$ in Dunham et al. (2010) and Klein et al. (2005), respectively. Assuming a temperature of 30 K, it corresponds to a luminosity of $2.2 \times 10^2 L_{\odot}$. The luminosities of IR1 and IR2 were estimated as $5.3 \pm 1.4 \times 10^3 L_{\odot}$ and $1.3 \pm 0.4 \times 10^3 L_{\odot}$, respectively, including the possible contribution of the cold component. The same method was employed for the estimation of the lower and upper limits in M8E. Note that, as mentioned in section 2, IR1 consists of the MYSO and the NIR object, and the flux contribution of the NIR object may not be negligible in the shorter MIR. Moreover, Rodon (2009) reported that the NIR emission of IR1 was detected only from the NIR object. In addition, an $11.2 \mu\text{m}$ image obtained by the RMS project (Lumsden et al. 2013) with United Kingdom Infrared Telescope/Mid-Infrared Imager/Echelle Spectrometer (UKIRT/MICHELLE) exhibited an extended IR1 structure. However, this structure is not observed in the $18 \mu\text{m}$ image, indicating that the NIR object dominates the flux densities of IR1 only at less than $18 \mu\text{m}$. Therefore, the minimum luminosity of the MYSO is decreased to $2.7 \times 10^3 L_{\odot}$, and its total luminosity becomes $4.7 \pm 2.0 \times 10^3 L_{\odot}$.

IR2 reached the ZAMS stage owing to the existence of the associating UCH II region (Kurtz et al. 1994). Its spectral type could be B2.5-3.5 (Thompson 1984) according to the derived luminosity ($1.3 \pm 0.4 \times 10^3 L_{\odot}$). This result is consistent with the estimation of the B2 spectral type derived from the measurement of the free-free emission reported by Kurtz, Churchwell, and Wood (1994). The mass is estimated as $6.5 \pm 0.5 M_{\odot}$ (Cox 2000). Conversely, the MYSO in IR1 is considered to be a pre-H burning object because of the absence of the UCH II region (Kurtz et al. 1994). Its lower limit of spectral type is established to be B1-2 and its mass is $9.5 \pm 1.5 M_{\odot}$, respectively (Thompson

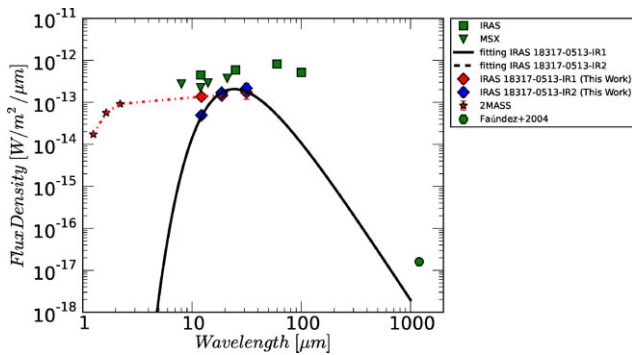


Fig. 7. Result of SED fitting to IRAS 18317–0513 IR1 and IR2. Red, blue, and green marks represent the flux densities of IR1, IR2, and the entire unresolved region, respectively. The flux densities obtained are plotted using diamond marks. The solid line represents the blackbody radiation fitting of IR1 and the dotted line represents that of IR2. Note that these two lines are overlapped because of almost similar results. The red dash-dotted line represents the linear fitting of IR1 at shorter wavelengths. (Color online)

1984; Cox 2000). The above estimation shows that the less-massive object, RAFGL 6366S-IR2, is located at a more evolved stage than the more-massive object, RAFGL 6366S-IR1.

3.3.3 IRAS 18317–0513

The SEDs of IRAS 18317–0513-IR1 and IRAS 18317–0513-IR2 are plotted in figure 7. The sum of our flux densities of IR1 and IR2 is almost consistent with that of the flux densities previously unresolved by IRAS (12 and 25 μm) and MSX (8, 12, 14, and 21 μm) (see figure 7). At wavelengths longer than 12 μm , the SED of IR2 was well reproduced by a single-temperature blackbody radiation with a temperature of 119 ± 4 K (dashed line in figure 7). The distance of IRAS 18317–0513 is 3.0 ± 0.58 kpc, as obtained in the RMS project (Urquhart et al. 2008; Lumsden et al. 2013). Therefore, the derived luminosity of IR2 was $2.4 \times 10^3 L_{\odot}$ with an error of 7%. For IR1, the obtained SED was flat from 12 to 31 μm (see figure 7). Therefore, it is not appropriate to estimate the luminosity by a single blackbody fitting. Conversely, the flux densities of IR1 at 18 and 31 μm were slightly similar to those of IR2. Therefore, the luminosity of IR1 at wavelengths longer than 31 μm was obtained assuming that it had a similar temperature to IR2, 119 ± 4 K, whereas that from 12 to 31 μm was derived using numerical integration. The estimated luminosity of IR1 is $2.7 \times 10^3 L_{\odot}$ with an error of 9%.

The flux densities at FIR wavelengths of 60 and 100 μm exhibited significant excess flux density; however, they were measured with larger beam sizes of $>1'$. In contrast, the excess 1.3 mm flux density was measured with a sufficiently small aperture of $24''$ for estimating the luminosity

(Faúndez et al. 2004). Assuming a temperature of 30 K, it corresponds to a luminosity of $5.9 \times 10^2 L_{\odot}$ with an assumed error of 50%. Additionally, this is considered as the uncertainty of the total luminosity of IR1 and IR2, i.e., $3.2 \pm 0.7 \times 10^3 L_{\odot}$ and $2.9 \pm 0.7 \times 10^3 L_{\odot}$, respectively. The same method was employed in the estimation of the lower and upper limits in M8E. Both IRAS 18317–0513-IR1 and IR2 seem to be pre-H burning objects because of the absence of UCH II regions (Urquhart et al. 2009). The lower limits of spectral type and mass of IR1 and IR2 were estimated as B1.5–2 ($8.5 \pm 0.5 M_{\odot}$) and B1.5–2.5 ($8 \pm 1 M_{\odot}$), respectively (Thompson 1984; Cox 2000). Thus, the two objects have similar masses and are located at almost similar evolutionary stages, and they would have formed almost simultaneously.

A summary of the estimated luminosity, masses, and spectral type is listed in table 7 for the three regions.

4 Discussion

4.1 Possible explanations of the different evolutionary stages observed

In the previous section, two out of the three observed regions indicated that the less-massive object was located at a more evolved stage than the more-massive object. Here, we first discuss other possible scenarios for the different evolutionary stages observed that do not need star-forming sequences, such as episodic accretion and binary systems. Finally, we discuss the “mass-sequential star formation” scenario in detail, which indicates that less-massive objects form earlier than more massive ones.

4.1.1 Episodic accretion in MYSOs

As described in the previous section, the above mass estimation assumes that the accretion rate of the MYSOs is almost constant. However, episodic accretion assumes a temporal and significant increase in the accretion luminosity. This is a well-known event that occurs in lower-mass-forming YSOs (Audard et al. 2014). Recently, such episodic accretion events have also been observed in MYSOs (Caratti o Garatti et al. 2017; Hunter et al. 2017; Burns et al. 2020; Uchiyama et al. 2020). Therefore, accidental episodic accretion is another possible scenario. In comparison with the previous photometry made by space telescopes, a large flux increment in the infrared does not occur for decades. Hence, an EXor-like burst, lasting up to several years, is not likely to occur. However, longer events such as FUor-like bursts cannot be ruled out by current observations. In such cases, MYSOs that are more luminous might be less massive than the objects with UCH II regions, and the different evolutionary stages observed do not indicate the

Table 7. Luminosities of objects and their estimated spectral types and masses.

Object	Evolutionary stage	Luminosity [L_{\odot}]	Spectral type	Mass [M_{\odot}]
M8E-IR	MYSO*	$2.8 \pm 0.7 \times 10^3$	B1.5-2.5	8.0 ± 0.5
M8E-radio	UCH II [†]	$1.2 \pm 0.7 \times 10^3$	B2.5-4	6.0 ± 1.0
RAFGL 6366S-IR1	MYSO*	$4.7 \pm 2.0 \times 10^3$	B1-2.5	9.5 ± 1.5
RAFGL 6366S-IR2	UCH II [†]	$1.3 \pm 0.4 \times 10^3$	B2.5-3.5	6.5 ± 0.5
IRAS 18317–0513-IR1	MYSO*	$3.2 \pm 0.7 \times 10^3$	B1.5-2	8.5 ± 0.5
IRAS 18317–0513-IR2	MYSO*	$2.9 \pm 0.7 \times 10^3$	B1.5-2.5	8 ± 1

Notes. *Current spectral types and masses are estimated for the MYSOs.

[†]Spectral types and masses are estimated assuming they are on the ZAMS for the objects with the UCH IIs.

mass-sequential star formation. However, if episodic accretion occur in both regions, it implies a high tendency of episodic accretion to form MYSOs, whereas that in lower-mass YSOs is indicated as less than 10% (Contreras Peña et al. 2017). Therefore, although the frequency of episodic accretion in MYSOs is not observationally clear at present, this situation seems to happen with less possibility. Further observational studies of episodic accretion in MYSOs are required in order to make a firm conclusion.

4.1.2 Binary system

The mass of each component is reduced when the MYSOs are not single objects but binary systems. If MYSOs are equal- or similar-mass binaries, the mass difference in the M8E region is small and all objects have slightly similar mass in the RAFGL 6366S region. Although the binary rate of MYSOs is currently unclear, a large spectroscopic binary survey of main-sequence O and B stars has shown that the close and similar-mass binary rate of all observed B0-3 stars is approximately 50% (Chini et al. 2012). The authors have suggested that most close binary systems tend to be similar-mass binary systems in massive stars. Therefore, it may happen in the observed regions that the observed MYSOs are not single MYSOs but binaries. Even if the MYSOs are binary, their total luminosities are more than two times higher compared to those of the objects with the UCH II regions in our samples. Then, the mass of the system will still be heavier in binary systems than in the objects with the UCH II regions, even though the MYSOs are equal mass binaries. Therefore, even in such a case, less-massive systems will be formed earlier than more massive systems in these two regions.

4.1.3 Mass-sequential star formation

Generally, it is accepted that the stellar evolution of less-massive objects takes a significantly longer time than that of more-massive objects during the formation (McKee & Tan 2002; Bonnell & Bate 2006; Zinnecker & Yorke 2007). Although the gas gathering time slightly depends

on the final stellar mass (McKee & Tan 2002), the contraction time strongly depends on it (Zinnecker & Yorke 2007). Therefore, less-massive objects evolve more slowly than more-massive objects during the evolution toward ZAMS. If both objects are formed simultaneously, or if the more-massive object had started formation earlier, the more-massive object should be located at a more evolved stage. However, our observations show opposite orders in two out of the three observed regions. Therefore, the less-massive objects should be formed earlier than the more-massive objects in these two regions. This trend suggests, for the first time, “mass-sequential star formation” in 0.1 pc scale massive star forming regions. Note that we also have to consider larger scale “mass-sequential star formation” in this situation. In target selection criteria, the regions which have clear cloud–cloud collision signature were excluded. However, 1 or 10 pc scale “mass-sequential star formation” cannot be ruled out completely, such as an ionization front passing through a molecular cloud which may condense the gas and trigger massive star formation as it goes. In fact, in the M8E region, an ionization front which is sweeping the gas away from the north-west to the south-east has been reported (Tiwari et al. 2020). This ionization front is driven by the larger-scale H II region of NGC 6530, and the larger-scale “mass-sequential star formation” due to the passing through of the ionization front is suggested from the observations of gas and lower-mass YSOs around M8E (Tiwari et al. 2020). It is notable that, in the other two regions, such a work is not available at present. Then, although it is not clear at present whether small or large scale “mass-sequential star formation” has taken place in the observed areas, it is remarkable that “mass-sequential star formation” can be found even in such a small, 0.1 pc sized, massive star-forming region.

4.2 Possible supports of mass-sequential star formation

Theoretically, the masses of cores in molecular clouds depend on the gas effective pressure of the clouds, namely

Jeans mass. To create and sustain massive cores, it is necessary to increase the effective pressure, and the possible mechanisms include outflows and/or jets, radiative heating from previously formed lower-mass YSOs, and magnetic field. Although the magnetic field is theoretically suggested to aid the formation of a massive core (Hennebelle et al. 2011), it creates various masses of YSOs simultaneously because of the spatial distribution of its strength and does not produce the suggested star-forming sequences. We discussed the possibility of feedback from previously formed lower-mass YSOs, such as radiative heating and outflows and/or jets, to explain “mass-sequential star formation” in the previous section.

4.2.1 Radiative heating

Radiative heating increases the thermal pressure of the gas in the massive star-forming regions. When radiative heating by the previously formed YSOs increases the thermal pressure sufficiently, it results in the formation of more-massive objects. This effect of radiative heating is theoretically suggested inside a massive core (Krumholz 2006), although it is unclear whether radiative energy from the less-massive object/core is enough to affect a larger region, that is, physically supporting an adjacent forming massive core.

For a brief estimation, we assume the case of the M8E region and that the cloud has a constant density and contains a single MYSO at the pre-H burning stage. A typical density of massive and dense molecular clouds, $n_{\text{H}_2} \sim 10^4 \text{ cm}^{-3}$ (Longmore et al. 2011), is assumed. We then solve the thermal equilibrium of heated dust from the previously formed MYSO assuming that the dust emissivity index, β , is 2, which is a typical observed value in massive star-forming regions (Hill et al. 2006). The radiation of the previously formed MYSO can be considered a blackbody at a core temperature, approximately 100 K (Kurtz et al. 2000; Churchwell 2002; Sridharan et al. 2002). The luminosity of the previously formed MYSO, M8E-radio, is $1.2 \times 10^3 L_{\odot}$, but the luminosity in the pre-H burning stage is considered to be lower (Palla & Stahler 1993; Hosokawa & Omukai 2009). We adopt a luminosity of $800 L_{\odot}$ in this calculation, corresponding to that at the birth line (Siess et al. 2000). Although the gas temperature should be higher than 40 K to form a core with a thermal Jeans mass of approximately $8.0 M_{\odot}$, corresponding to the mass of the lately formed M8E-IR, the temperature at which M8E-IR is located is slightly lower (29 K). According to observations (Kurtz et al. 2000; Sridharan et al. 2002; Grave & Kumar 2009), the temperature of the MYSO core may vary in from 50 to 200 K. However, this variation alone cannot increase the gas temperature sufficiently; it increases only up to 36 K with a fixed luminosity. This effect is not negligible; however, it seems to be insufficient to provide the

sole explanation in terms of the radiative heating from lower-mass YSOs. Another support which can help the formation of massive cores may also be effective in such a case.

In very recent radio observations in M8E, a dense gas temperature of approximately 80 K was reported; this requires some heating mechanism, although this value includes heating from M8E-IR and M8E-radio (Tiwari et al. 2020). Tiwari et al. (2020) proposed external heating from NGC 6530, which is located north-west of the M8E region; however, further observational investigation is needed to reveal the detailed star formation history in the M8E region.

4.2.2 Outflows and/or jets

Turbulent-supported cores have been suggested theoretically with regard to cluster formation, and they are referred to as the “turbulent fragmentation” model (Padoan & Nordlund 2002). Outflows and/or jets of previously formed YSOs can add extra turbulence and increase the effective gas pressure locally, and the resulting star-forming sequences can be obtained when the additional pressure is sufficiently large to produce more-massive objects. In fact, some star formation and star-forming cores in pc- or 10 pc-scale sized regions would be controlled by turbulence; for instance, Ophiuchus (Zhang et al. 2015). Therefore, this mechanism might be effective to some extent; however, the universality of its effect from the core to cloud scale is unclear.

Our observational study reveals, for the first time, the possibility of star-forming sequences of star-forming cores on a 0.1 pc-scale and for massive objects. Local feedback from the previously formed YSOs may trigger the creation of a more massive core and hence a star. Much larger scale “mass-sequential star formation”, such as an ionization front passing through star-forming regions, may also be accountable. More observations in the MIR and other wavelengths in small-scale massive star-forming regions are required to study this mechanism statistically and examine other possible scenarios.

5 Conclusion

In this study, three compact massive star-forming regions, namely M8E, RAFGL 6366S, and IRAS 18317–0513, were observed in the MIR at 31 and 37 μm to study star-forming sequences. MAX38 mounted on the miniTAO telescope was used in this study. The spatial resolution in our observations was approximately 8'' at 31 μm and 9'' at 37 μm , which is the highest resolution at wavelengths longer than 30 μm among the other observations carried out and is sufficiently high to resolve individual objects in the observed regions. The obtained images enabled us to measure the infrared luminosity of each object separately.

Individual stellar masses were estimated from the derived luminosities using stellar models. In M8E and RAFGL 6366S, the objects associated with the UCH II regions have lower masses compared to those without UCH II regions. We considered possible explanations for this observed difference in evolutionary stages in small regions. Although the episodic accretion of MYSOs and the existence of binary systems could affect mass estimation, mass-sequential star formation in small-scale massive star-forming regions is suggested for the first time. This is because less-massive YSOs have longer star-formation timescales and were formed before the more massive ones. This suggests that some feedback mechanisms such as outflows and/or jets and/or radiative heating by the previously formed less-massive object enhanced the formation of the more-massive object on a small scale.

Our results indicate the potential of high spatial-resolution observations in the MIR, including 31 and 37 μm . In the near future, a high spatial-resolution MIR imaging survey of high-mass star-forming regions with TAO/MIMIZUKU will extend our results.

Acknowledgments

We are grateful to all the TAO project members, including the members in Chile, for their kind support. We would like to thank Assoc. Prof. Naoto Kobayashi for insightful discussions and comments. We also acknowledge APEX, which provided very useful archives of weather data. We thank Dinesh Shenoy and Roberta M. Humphreys for providing information on the data obtained by SOFIA/FORCAST. This work was supported by Grant-in-Aid for Japan Society for the Promotion of Science (JSPS) Fellows No.14-10274 (P.I. Uchiyama M.), Ministry of Education, Culture, Sports, Science and Technology (MEXT)/JSPS Grant-in-Aid for Scientific Researches (A) No.22253002 (P.I. Yoshii Y.), and Grant-in-Aid for Young Scientists (A) No.21684006 (P.I. Miyata, T.). The mini-TAO telescope operates in the Parque Astronómico Atacama in northern Chile under the auspices of Programa de Astronomía, a program of the Comisión Nacional de Investigación Científica y Tecnológica de Chile (CONICYT). This paper made use of information from the Red MSX Source survey database (http://rms.leeds.ac.uk/cgi-bin/public/RMS_DATABASE.cgi) which was constructed with support from the Science and Technology Facilities Council of the UK.

References

- Asano, K., et al. 2012, *Proc. SPIE*, 8446, 844634
- Audard, M., et al. 2014, in *Protostars and Planets VI*, ed. H. Beuther et al. (Tucson: University of Arizona Press), 387
- Bonnell, I. A., & Bate, M. R. 2006, *MNRAS*, 370, 488
- Bronfman, L., Nyman, L.-Å., & May, J. 1996, *A&AS*, 115, 81
- Burns, R. A., et al. 2020, *Nature Astron.*, 4, 506
- Caratti o Garatti, A., et al. 2017, *Nature Phys.*, 13, 276
- Carpenter, J. M., Snell, R. L., & Schloerb, F. P. 1995, *ApJ*, 445, 246
- Chini, R., Hoffmeister, V. H., Nasser, A., Stahl, O., & Zinnecker, H. 2012, *MNRAS*, 424, 1925
- Churchwell, E. 2002, *ARA&A*, 40, 27
- Cohen, M., Walker, R. G., Carter, B., Hammersley, P., Kidger, M., & Noguchi, K. 1999, *AJ*, 117, 1864
- Contreras Peña, C., et al. 2017, *MNRAS*, 465, 3011
- Cox, A. N. ed. 2000, *Allen's Astrophysical Quantities*, 4th ed. (New York: Springer)
- Damiani, F., Prisinzano, L., Micela, G., & Sciortino, S. 2019, *A&A*, 623, A25
- de Wit, W. J., et al. 2009, *A&A*, 494, 157
- Dunham, M. K., et al. 2010, *ApJ*, 717, 1157
- Faúndez, S., Bronfman, L., Garay, G., Chini, R., Nyman, L.-Å., & May, J. 2004, *A&A*, 426, 97
- Foster, J. B., et al. 2014, *ApJ*, 791, 108
- Grave, J. M. C., & Kumar, M. S. N. 2009, *A&A*, 498, 147
- Güsten, R., Nyman, L. Å., Schilke, P., Menten, K., Cesarsky, C., & Booth, R. 2006, *A&A*, 454, L13
- Hennebelle, P., Commerçon, B., Joos, M., Klessen, R. S., Krumholz, M., Tan, J. C., & Teyssier, R. 2011, *A&A*, 528, A72
- Hill, T., Thompson, M. A., Burton, M. G., Walsh, A. J., Minier, V., Cunningham, M. R., & Pierce-Price, D. 2006, *MNRAS*, 368, 1223
- Hofner, P., Wyrowski, F., Walmsley, C. M., & Churchwell, E. 2000, *ApJ*, 536, 393
- Hosokawa, T., & Omukai, K. 2009, *ApJ*, 691, 823
- Hunter, T. R., et al. 2017, *ApJ*, 837, L29
- Issac, N., Tej, A., Liu, T., Varricatt, W., Vig, S., Ishwara Chandra, C. H., Schultheis, M., & Nandakumar, G. 2020, *MNRAS*, 497, 5454
- Kaeufl, H. U., Bouchet, P., van Dijsseldonk, A., & Weilenmann, U. 1991, *Exp. Astron.*, 2, 115
- Kim, K.-T., & Koo, B.-C. 2001, *ApJ*, 549, 979
- Klein, R., Posselt, B., Schreyer, K., Forbrich, J., & Henning, T. 2005, *ApJS*, 161, 361
- Konishi, M., et al. 2015, *PASJ*, 67, 4
- Krumholz, M. R. 2006, *ApJ*, 641, L45
- Kurtz, S., Cesaroni, R., Churchwell, E., Hofner, P., & Walmsley, C. M. 2000, in *Protostars and Planets VI*, ed. H. Beuther et al. (Tucson: University of Arizona Press), 299
- Kurtz, S., Churchwell, E., & Wood, D. O. S. 1994, *ApJS*, 91, 659
- Lagadec, E., et al. 2011, *MNRAS*, 417, 32
- Linz, H., et al. 2009, *A&A*, 505, 655
- Liu, J., Zhang, Q., Qiu, K., Liu, H. B., Pillai, T., Girart, J. M., Li, Z.-Y., & Wang, K. 2020, *ApJ*, 895, 142
- Longmore, S. N., Pillai, T., Keto, E., Zhang, Q., & Qiu, K. 2011, *ApJ*, 726, 97
- Lumsden, S. L., Hoare, M. G., Urquhart, J. S., Oudmaijer, R. D., Davies, B., Mottram, J. C., Cooper, H. D. B., & Moore, T. J. T. 2013, *ApJS*, 208, 11
- McKee, C. F., & Tan, J. C. 2002, *Nature*, 416, 59
- Minezaki, T., et al. 2010, *Proc. SPIE*, 7733, 773356
- Miyata, T., et al. 2012, *Proc. SPIE*, 8444, 84446B
- Monnier, J. D., Geballe, T. R., & Danchi, W. C. 1998, *ApJ*, 502, 833
- Mottram, J. C., Hoare, M. G., Lumsden, S. L., Oudmaijer, R. D., Urquhart, J. S., Sheret, T. L., Clarke, A. J., & Allsopp, J. 2007, *A&A*, 476, 1019
- Mueller, K. E., Shirley, Y. L., Evans, N. J., II, & Jacobson, H. R. 2002, *ApJS*, 143, 469
- Nakamura, T. 2011, PhD thesis, The University of Tokyo

- Nakamura, T. 2012, PhD thesis, The University of Tokyo
- Nakamura, T., et al. 2010, *Proc. SPIE*, 7735, 773561
- Nakamura, T., Miyata, T., Sako, S., Kamizuka, T., Asano, K., Uchiyama, M., & Okada, K. 2016, *Proc. SPIE*, 9908, 99082U
- Padoan, P., & Nordlund, Å. 2002, *ApJ*, 576, 870
- Palla, F., & Stahler, S. W. 1993, *ApJ*, 418, 414
- Papoular, R. 1983, *A&A*, 117, 46
- Peretto, N., et al. 2020, *MNRAS*, 496, 3482
- Peretto, N., & Fuller, G. A. 2009, *A&A*, 505, 405
- Qiu, K., Zhang, Q., & Menten, K. M. 2011, *ApJ*, 728, 6
- Reid, M. J., Menten, K. M., Brunthaler, A., Zheng, X. W., Moscadelli, L., & Xu, Y. 2009, *ApJ*, 693, 397
- Rodon, J. A. 2009, PhD thesis, Max-Planck-Institut für Astronomie
- Sako, S., et al. 2012, *Proc. SPIE*, 8450, 84503V
- Siess, L., Dufour, E., & Forestini, M. 2000, *A&A*, 358, 593
- Simon, M., Cassar, L., Felli, M., Fischer, J., Massi, M., & Sanders, D. 1984, *ApJ*, 278, 170
- Smith, B. J., Leisawitz, D., Castelaz, M. W., & Luttermoser, D. 2002, *AJ*, 123, 948
- Sridharan, T. K., Beuther, H., Schilke, P., Menten, K. M., & Wyrowski, F. 2002, *ApJ*, 566, 931
- Stephens, I. W., Jackson, J. M., Sanhueza, P., Whitaker, J. S., Hoq, S., Rathborne, J. M., & Foster, J. B. 2015, *ApJ*, 802, 6
- Tan, J. C., Beltrán, M. T., Caselli, P., Fontani, F., Fuente, A., Krumholz, M. R., McKee, C. F., & Stolte, A. 2014, in *Protostars and Planets VI*, ed. H. Beuther et al. (Tucson, AZ: University of Arizona Press), 149
- Thompson, R. I. 1984, *ApJ*, 283, 165
- Tiwari, M., Menten, K. M., Wyrowski, F., Giannetti, A., Lee, M. Y., Kim, W. J., & Pérez-Beaupuits, J. P. 2020, *A&A*, 644, A25
- Tothill, N. F. H., Gagné, M., Stecklum, B., & Kenworthy, M. A. 2008, in *Handbook of Star Forming Regions, Volume I: The Northern Sky*, Vol. 4., ed. B. Reipurth (San Francisco: ASP), 533
- Uchiyama, M., et al. 2020, *PASJ*, 72, 4
- Urquhart, J. S., et al. 2008, *A&A*, 487, 253
- Urquhart, J. S., et al. 2009, *A&A*, 501, 539
- Walsh, A. J., Burton, M. G., Hyland, A. R., & Robinson, G. 1998, *MNRAS*, 301, 640
- Wang, Y., et al. 2011, *A&A*, 527, A32
- Wang, Y., Beuther, H., Zhang, Q., Bik, A., Rodón, J. A., Jiang, Z., & Fallscheer, C. 2012, *ApJ*, 754, 87
- Yuasa, M., Unno, W., & Magono, S. 1999, *PASJ*, 51, 197
- Zhang, G., Li, D., Hyde, A. K., Qian, L., Lyu, H., & Wu, Z. 2015, *Sci. China Phys Mech. Astron.*, 58, 5561
- Zinnecker, H., & Yorke, H. W. 2007, *ARA&A*, 45, 481